PAPER • OPEN ACCESS

Phase-field study on microstructure formation in Mar-M247 during electron beam welding and correlation to hot cracking susceptibility

Phase-field study on microstructure formation in Mar-M247 during electron beam welding and correlation to hot cracking susceptibility

B Böttger[1], M Apel[1], T Jokisch[2] and A Senger[3]

[1] Access e.V., Aachen, Germany
[2] Siemens AG, Gas and Power, Germany
[3] Institut für Schweißtechnik und Fügetechnik (ISF), RWTH Aachen, Germany

E-mail: b.boettger@access.rwth-aachen.de

Abstract. Ni-base superalloys are frequently used for cast components in the aero-engine and power generation industries. For joining and repair of these components, beam welding is often the method of choice in industrial praxis. However, precipitation-strengthened nickel alloys generally present poor weldability as a consequence of their high weld cracking susceptibility, with high segregating alloys like Mar-M247 even being considered unweldable. Therefore, strong efforts are taken on optimizing techniques and parameters to reduce crack formation during welding of these alloys. Optimization of welding parameters can be assisted by virtual modelling methods through different scales. To be able to focus onto the factors which eventually are responsible for crack formation during welding, comprehensive modelling of the whole process chain is required, starting from a realistic model of the base material and a simulation of the heat source on the macro-scale, and including melting and microstructure formation during welding on the micro-scale. Then, based on the thermal history and the exact microstructure, cracking susceptibilities during solidification can be deduced by hot cracking models adapted to the specific conditions. In this paper, results of microstructure simulations are presented for the technical superalloy MAR-M247 using the phase-field software MICRESS with coupling to Calphad databases. Based on prior phase-field simulations of equiaxed and columnar microstructures of the base material as well as results of a macroscopic simulation of the heat source, melting and subsequent solidification of MAR-M247 has been simulated for two different welding parameter sets. As-weld microstructures are compared to experimental welds, and the virtual hot cracking susceptibility, obtained from the simulation results using a modified Rappaz–Drezet–Gremaud (RDG) hot cracking criterion, is discussed against experimental crack observations.

1. Introduction

Phase-field models have become very popular for simulation of microstructure evolution in material processing. While solidification and phase transformations of alloys have been widely addressed using different approaches [1-3], relatively little simulation work has been done on microstructure development during welding processes. This may be due to specific challenges like the complex thermal conditions which lead to partial melting and subsequent re-solidification, the requirement of defining a realistic initial microstructure with a different typical length scale, the complex conditions how melting leads to formation of new grains, and not to forget the complex alloy chemistry which is involved in may technical welding problems [4].

The software MICRESS® [5] is based on the phase-field concept for multiphase systems which has been extended to multicomponent systems by direct coupling to thermodynamic databases [3, 6]. Since then, the software has been continuously developed not only for advanced scientific applications but also as a simulation tool for microstructure formation in technical processes [7-9].

In this paper, microstructure simulations for welding of Mar-M247 are presented (section 3.4), which have been obtained for two different welding speeds (1 mm/s, 6 mm/s) and two different morphologies (DS, CC) of the base material. While this base material (section 3.3) as well as the welding process at microscale has been simulated using the software MICRESS®, the temperature field and its change in time have been modelled at the macroscopic scale as shown in section 2 using Ansys Version 17.2. The simulated welding microstructures are compared with experimental micrographs obtained under identical conditions. Finally, the hot-cracking susceptibility has been modelled based on the microstructure simulation results using a modified RDG [10-11] criterion and discussed against experimental cracking statistics.

2. Thermal modelling of the welding process

Due to high process complexity, the equivalent heat source (EHS) method is used for the mathematical representation of a location and time-dependant heat effect of an electron beam welding process on Mar-M247. This allows a close representation of temperature distribution in the component. For this purpose, the EHS and the temperature field are adapted and calibrated on the basis of experimental data. The geometric and energetic components of the heat source are set by the solidus line (cross sections) between the base material and the seam and the temperature on the surfaces (measured temperatures via thermocouples during welding process). Due to atypical seam depth to seam width ratio of the electron beam weld at lower welding speeds, a modification of the characteristic beam EHS is necessary [12]. In contrast to the usual high speed beam processes, an extended energy distribution over the seam depth is required. Heat sources used for the phase field simulations are based on a multi-stage approach. The different energy distribution over the depth is varied in the 3D heat source by intensity factors:

$$Q_{TH} = \frac{3\eta_{TH} p_{nom} k_{eff}}{\pi R_{TH}^2 H} step\left(\frac{H-z}{1[mm]}\right) I \exp\left(-\frac{3}{R_{TH}^2}\left((x-x_0)^2 + (y-y_0)^2\right)\right) \quad (1)$$

with energy quota η_{TH}, radius of the stepwise deep weld heat source R_{TH}, nominal power P_{nom}, stepwise energy distribution over the depth I and process efficiency k_{eff}.
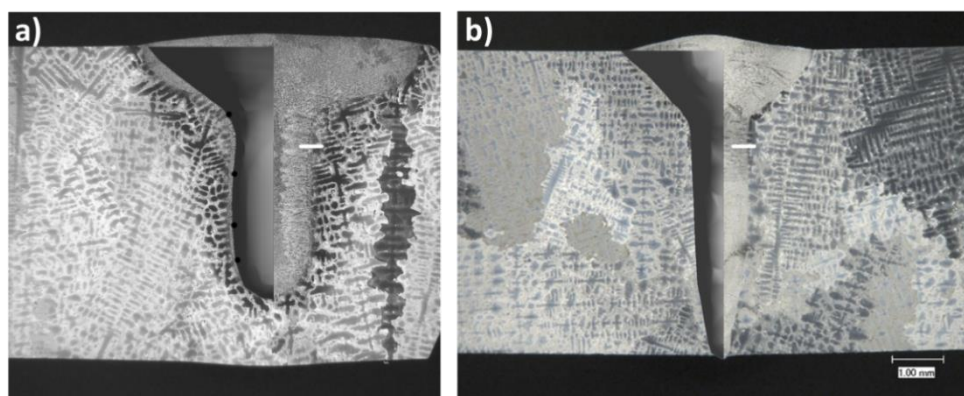

Figure 1. Simulated and observed fusion zones for a welding speed of (a) 1 mm/s, and (b) 6 mm/s. The white lines indicate the position of the results shown in figure 4.

For better temperature distribution near the surface the 3D heat source is superposed with a 2D heat source with exponent 10:

$$Q_{SH} = \beta \frac{\eta_{SH} \, 3 p_{nom} \, k_{eff} \, 0.727}{\pi \, R_{SH}^2} \exp\left(-\left(\frac{2}{R_{ES}^2}\left((x-x_0)^2 + (y-y_0)^2\right)\right)^5\right) \tag{2}$$

with energy quota η_{SH}, radius of the surface heat source R_{ES} and longitudinal energy distribution (degree of asymmetry) β. The good agreement between the simulated and the experimental fusion zone in figure 1 is essentially defined by the intensity factor.

3. Phase-field modelling

3.1. Multiphase-field model and MICRESS® software

The multiphase-field theory describes the evolution of multiple phase-field parameters $\phi_\alpha(\vec{x},t)$ in time and space. They reflect the spatial distribution of multiple grains with different orientation and/or of multiple phases with different thermodynamic properties. At the interfaces, the phase-field variables change continuously over an interface thickness η which can be large compared to the atomic interface thickness but small compared to the microstructure length scale. Their time evolution is calculated by a set of phase-field equations derived by the minimization of the free energy functional [3]:

$$\dot{\phi}_\alpha = \sum_{\beta \neq \alpha}^{v} M_{\alpha\beta}\left[\frac{\sigma_{\alpha\beta}}{v}\left(\frac{1}{2}\left(\nabla^2\phi_\alpha - \nabla^2\phi_\beta\right) + \frac{\pi^2}{2\eta_{\alpha\beta}^2}\left(\phi_\beta - \phi_\alpha\right)\right) + \sum_{\gamma \neq \alpha \neq \beta}^{n} J_{\alpha\beta\gamma} + |\nabla\phi|\Delta_{\alpha\beta}\right] \tag{3}$$

with $J_{\alpha\beta\gamma}$ being higher order terms which account for the interaction with additional phases γ in triple or multiple phase regions:

$$J_{\alpha\beta\gamma} = \frac{1}{2}(\sigma_{\beta\gamma} - \sigma_{\alpha\gamma})\left(\frac{\pi^2}{\eta^2}\phi_\gamma + \nabla^2\phi_\gamma\right) \tag{4}$$

$$M_{\alpha\beta} = \tilde{M}_{\alpha\beta}\frac{8\eta}{\pi^2} \tag{5}$$

For sake of simplicity, only the isotropic formulation is shown here. The corresponding equations including anisotropy of the interface energy σ and kinetic constants $M_{\alpha\beta}$ are given in [13]. Furthermore, a correction on the interface mobility has been applied to account for the finite interface thickness [14] (sometimes denoted as "quantitative" phase-field model).

In equation (3), $M_{\alpha\beta}$ is the mobility of the interface as a function of the interface orientation, described by the normal vector $\vec{n}$. $\sigma^*_{\alpha\beta}$ is the anisotropic surface stiffness, and $K_{\alpha\beta}$ is related to the local curvature of the interface. The interface, on the one hand, is driven by the curvature contribution $\sigma^*_{\alpha\beta}K_{\alpha\beta}$ and on the other hand by the thermodynamic driving force $\Delta_{\alpha\beta}$. This driving force which is a function of temperature T and local composition $\vec{c}$ couples the phase-field equations to the multi-phase diffusion equations

$$\dot{\vec{c}} = \nabla\sum_{\alpha=1}^{N}\phi_\alpha\vec{D}_\alpha\nabla\vec{c}_\alpha \qquad \text{with } \vec{c} \text{ defined by} \qquad \vec{c} = \sum_{\alpha=1}^{N}\phi_\alpha\vec{c}_\alpha \tag{6}$$

and $\vec{D}_\alpha$ being the multicomponent diffusion coefficient matrix for phase α. $\vec{D}_\alpha$ and $\Delta_{\alpha\beta}$ are calculated online from databases for the given concentration and temperature.

The above equations are implemented in the software package MICRESS® [5] being used for the simulations throughout this paper. Direct coupling to thermodynamic and mobility databases is accomplished via the TQ-interface of Thermo-Calc Software [15]. The thermodynamic driving force ΔG and the solute partitioning are calculated separately using the quasi-equilibrium approach [3], and are introduced into the equation for the multiple phase-fields (equation (3)).

3.2. Model parameters and data

Thermodynamic data were provided by online coupling to the database TTNI7 [16] using the elements given in table 1 and the phases in table 2. In similar way, diffusion data for γ including cross-terms were taken from the MOBNI1 mobility database [15]. As for γ' no diffusion data is given in MOBNI1, values were read from a table as function of temperature also with all cross-terms. This table had been created before by a solidification simulation for Mar-M247 using the databases TCNI7/MOBNI2.

Compositions of both materials are shown in table 1. Phase-related data like nucleation conditions and interface energy data (σ) are given in table 2. Physical interface mobility values μ were taken sufficiently large to ensure diffusion limited growth and corrected for finite interface thickness artefacts using mobility correction [14]. The effects of fluid flow have been neglected.

Table 1: Chemical compositions (in wt. %) of the materials considered in the simulation.

	C	Cr	Co	Mo	W	Ti	Al	B	Ta	Hf
Mar-M247 CC	0.07	8.0	9.0	0.4	9.3	0.6	5.45	0.01	3.1	1.2
Mar-M247 DS	0.1	8.1	9.2	0.5	9.3	0.7	5.6	0.02	3.2	1.4

Table 2: Phases and phase related parameters

No	name in database [15]	identity/ constitution	diffusion data	nucleation in phase	$\mu_{0/x}$ (cm^4/Js)	$\mu_{1/x}$ (cm^4/Js)	$\sigma_{0/x}$ / (J/cm^2)	$\sigma_{1/x}$ / (J/cm^2)
0	LIQUID	melt	10^{-6} cm^2/s	1 (region)	-	0.1	-	2×10^{-5}
1	FCC_A1#1	γ	MOBNI1	0	0.1	1×10^{-7}	2.0×10^{-5}	1.0×10^{-5}
2	FCC_A1#2	(Hf,Ta)C	-	0,1	0.1	1×10^{-7}	1.2×10^{-4}	1.2×10^{-4}
3	MB2_C32	(Ti,Hf)B$_2$	-	0,1	0.1	1×10^{-7}	1.0×10^{-4}	1.0×10^{-4}
4	FCC_L12	γ'	MOBNI2	0,1	0.1	1×10^{-7}	2.0×10^{-5}	4.0×10^{-5}
5	M2B_TETR	(Cr,Mo,W)$_2$B	-	-	0.1	1×10^{-7}	1.0×10^{-4}	1.0×10^{-4}
6	M23C6	(Cr,MoW)$_{23}$C$_6$	-	-	0.1	1×10^{-7}	1.0×10^{-4}	1.0×10^{-4}

3.3. Initial microstructure

In view of the complexity of their microstructures, the small size of precipitates, and the difficulty to obtain concentration distributions in consistency with the nominal alloy composition, initial microstructures of the base metal were not taken from metallographic images. Instead, microstructures were obtained from 2D phase-field simulations of solidification with subsequent solution heat treatment according to the material specification. For the equiaxed base material, simulation was done at the scale of two ¼ equiaxed grains including a grain boundary and using the parameter sets given in table 1 and 2. A self-consistent homoenthalpic approach [17] was applied to ensure that microstructure formation was consistent with the macroscopic temperature boundary condition which leads to a realistic initial microstructure.

The columnar initial microstructure was simulated starting with dendrite selection in a temperature gradient of 75 K/cm (domain size 2000 x 2000, Δx=0,5 μm). After stationary growth was reached (figure 3(a)), the lower half of the domain was extracted, and solidification was completed (figure 3(b)) by further cooling with 0.6 K/s without following the dendrite tips (i.e. without co-moving frame).

In both the columnar and the equiaxed case, solidification conditions have been chosen such as to obtain a realistic primary and secondary dendrite arm spacing matching experimental data. A solution heat treatment according to the specifications of the material provider has been added. As visible in figure 2(d), the primary γ'-phase, which forms during solidification due to segregation of γ' forming elements, was not completely dissolved during heat treatment in case of the equiaxed alloy.
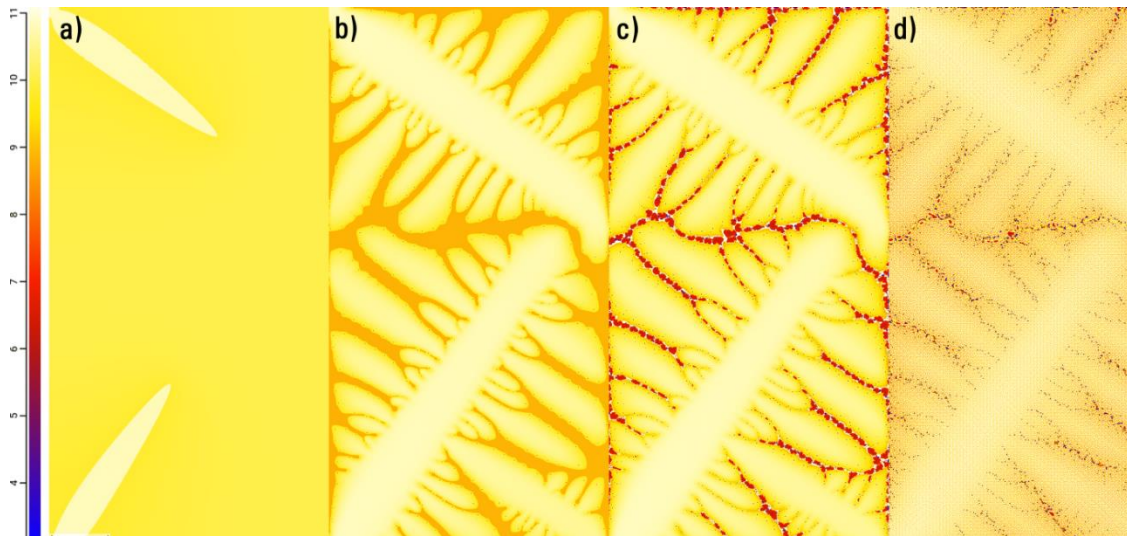
Figure 2. Development of equiaxed microstructure during different processing steps: (a)-(b) during solidification (c) after complete solidification (d) after solution heat treatment. Shown is the concentration distribution of Co. MC carbides and γ'-precipitates appear as dark and red, respectively.
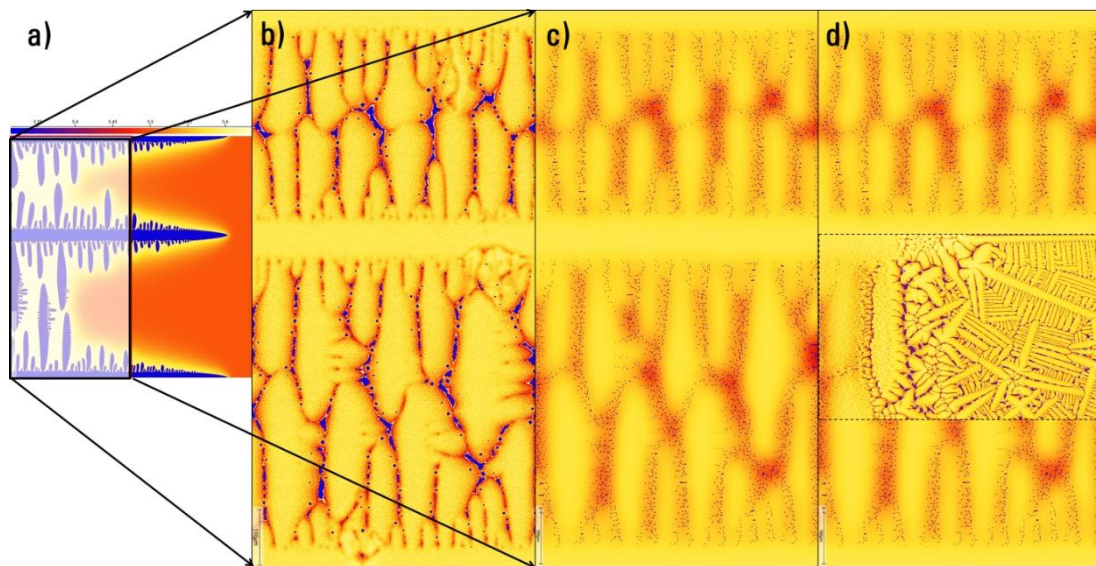

Figure 3. Simulation of directional initial microstructure during different processing steps: (a) Simulation for selection of primary dendrite spacing, (b) after complete solidification of lower half of the domain in (a), (c) after solution heat treatment, (d) subdomain for welding simulation (inserted microstructure is for welding speed 1 mm/s). Shown is the concentration distribution of Co.

3.4. Simulation of welding

As indicated in figure 3(d), a part of the domain has been extracted for the simulation of welding. However, welding microstructures are expected to be substantially finer than the normal solidification microstructures shown in figures 2 and 3. Simulating initial microstructures with a grid resolution sufficient for welding ($\Delta x <\sim 0.2$ μm) would not have been feasible. Therefore, the initial microstructure was interpolated to a three times finer resolution ($\Delta x = 0.167$ μm) using a functionality which refines and reconstructs the phase interfaces by use of the phase-field and diffusion equations.

For simulation of welding, one-dimensional temperature profiles were extracted from the temperature simulations of section 2 (at the positions corresponding to the white lines in figure 1). Simulation comprises melting of the base material, reversal of the front direction shortly before full melting, and re-solidification from the remaining solid (dendrites as well as detached fragments). Melting was initiated by nucleation of liquid phase, "reusing" grain number 0 in order to avoid grain boundaries between different melt "grains". During melting, large numbers of dendrite fragments are formed. In order to allow new grains emerge from these fragments, their complete detachment is detected, a new grain number was assigned, and random rotation of orientation was applied.

Simulation results for the equiaxed base material and two different welding speeds are shown in figure 4 in direct comparison to experimental micrographs obtained under identical conditions. A good qualitative agreement has been found in both cases.
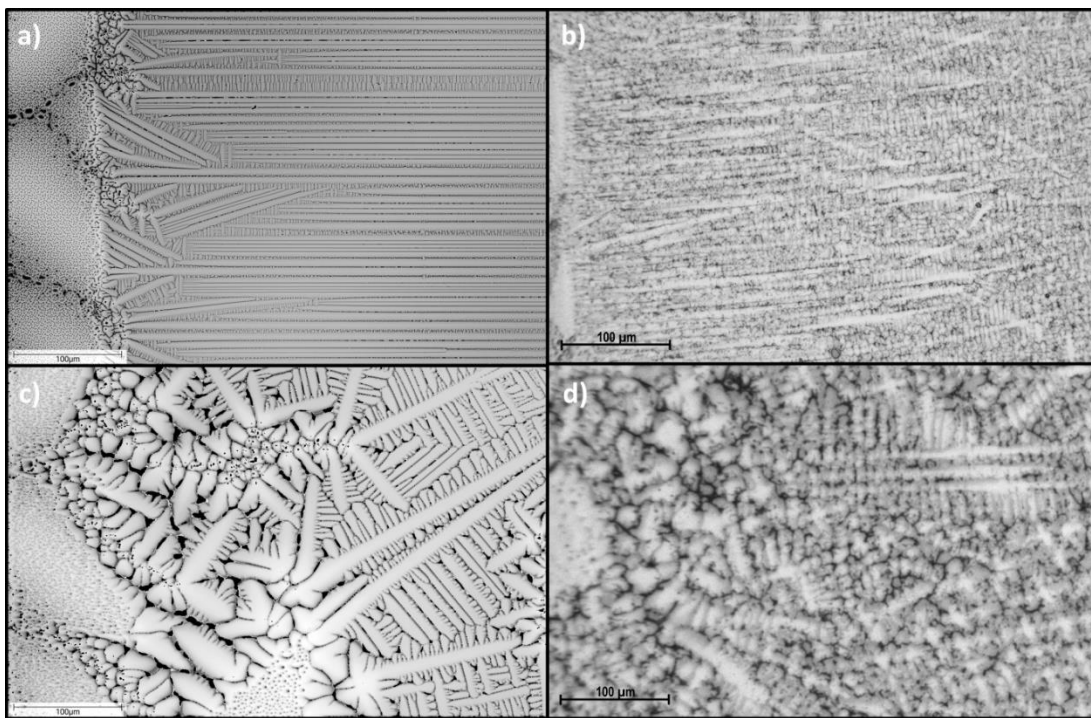

Figure 4. Comparison of simulated microstructures (left) and experimental micrographs (right) for Mar-M247 CC using a welding speed of 6 mm/s (a)-(b) and 1 mm/s (c)-(d)

4. Evaluation of hot-cracking susceptibility

According to Rappaz *et al.* [10] hot-cracking occurs due to insufficient feeding of liquid into strained interdendritic regions and is initiated if a critical strain rate $(d\varepsilon/dt)_{crit}$ is exceeded:

$$(d\varepsilon/dt)_{crit} = \frac{G}{(1+\beta)B}\left[\frac{\lambda_2^2 G \Delta p_{max}}{180\mu} - v_T \beta A\right] \text{ with } A = \int_{T_c}^{T_l}\frac{(1-f_s)f_s^2}{(1-f_s)^3}dT \text{ , } B = \int_{T_c}^{T_l}\frac{f_s^2}{(1-f_s)^3}\left(\int_{T_c}^{T}f_s dT\right)dT \quad (7)$$

Here, G is the temperature gradient, β the volume shrinkage due to solidification, v_T the solidification speed, μ the melt viscosity, and A and B are integrals over different functions of the fraction solid f_s. The coalescence temperature T_c, which typically is estimated as the temperature for $f_s = 99\%$, and the liquidus temperature T_l are used as integration limits. G, f_s as function of temperature, and the secondary arm spacing λ_2 were statistically evaluated from the simulation results as a function of the distance x from the left border of the simulation domain (table 3). For λ_2, a linear regression was calculated from 3 averaged values for different ranges of x (<200 μm, 200-300 μm,>300 μm). The maximum pressure drop Δp_{max} in equation (7) was estimated as shown below.

$(d\varepsilon/dt)_{crit}$ appears to be of little use comparing the risk of hot-cracking under different conditions, if the strains occurring during the welding process are unknown. Instead, $(d\varepsilon/dT)_{crit} = (d\varepsilon/dt)_{crit}/(dT/dt)$ seems to be more useful in this case [19] as strains are mainly caused by cooling and thus depend on the cooling rate $\dot{T}$. The alternative criterion $(d\varepsilon/dT)_{crit}$ has the units of a thermal expansion coefficient, and its magnitude should be closely related to this material constant. This assumption is very helpful for estimating the remaining unknown Δp_{max}: While the value of Δp_{max} in conventional casting typically is estimated as the sum of the atmospheric and metallostatic pressure [10, 11], in vacuum electron beam melting both quantities are negligibly small. Instead, we assume some pressure must build up in the already interconnected mushy zone at the center of the weld pool, e.g. by thermal contraction or clamping of the specimen. If we further assume that for slow welding (CC, 1 mm/s) there is just no hot-cracking (cf. figure 6), $(d\varepsilon/dT)_{crit}$ at the worst position x should be equal to the thermal expansion coefficient $(d\varepsilon/dT$ (Ni) $\sim 10^{-5}$ K^{-1}). By this way, Δp_{max} can be estimated to 1.1×10^6 Pa.

Table 3: Parameters for equation (7)

	CC, 1 mm/s	DS, 1 mm/s	CC, 6 mm/s	DS, 6 mm/s
$\lambda_2/\mu m$	12,80 -0,0144x	12,23 -0,0082x	2,85 +0,00074x	3,21 -0,00062x
β	0,13 (Calculated using Thermo-Calc and database TCNI9 [15])			
G/Kcm^{-1}	evaluated at $f_s=0.99$ for each timestep			
$\mu/kg(ms)^{-1}$	0.0032 [18]			
$\Delta p_{max}/Pa$	1.1×10^6 (calibrated, see text)			

With this knowledge, finally, the different welding conditions can be compared. Figure 5 shows $(d\varepsilon/dT)_{crit}$ as function of the distance (from the left side of the simulation domain, in cm). In case of the equiaxed material and a welding speed of 1 mm/s, $(d\varepsilon/dT)_{crit}$ shows a minimum close to the edge of the weld seam, with a value of $\sim 10^{-5}$ K^{-1} in accordance with the calibration of Δp_{max} (figure 5(a)). Higher values elsewhere indicate a lower hot-cracking risk at other distances.
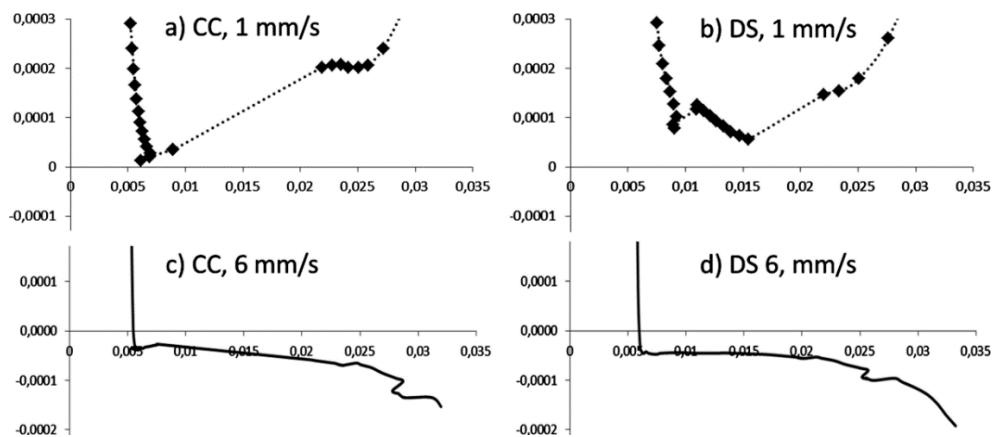

Figure 5. Comparison of $(d\varepsilon/dT)_{crit}$ (as function of the distance from the left side of the simulation domain in cm) for the different welding conditions indicating a low hot cracking risk for a welding speed of 1 mm/s and a high hot cracking risk for 6 mm/s

For the columnar material at 1 mm/s, using the same Δp_{max}, a similar curve of $(d\varepsilon/dT)_{crit}$ is obtained, indicating even a slightly lower risk of hot-cracking (higher minimum value of $(d\varepsilon/dT)_{crit}$, figure 5(b)). However, when changing to a welding speed of 6 mm/s, the behavior changes drastically as the $(d\varepsilon/dT)_{crit}$ curves for both materials go far to the negative for all simulated positions inside the weld pool. This indicates a strongly higher hot-cracking risk predicted by the $(d\varepsilon/dT)_{crit}$ criterion (essentially it means that even negative strain rates would be required to prevent cracking!) and is in good agreement with

cracking statistics carried out at Siemens AG for various welding speeds (figure 6). It should be noted that even when we would assume some dynamic pressure build-up at the center of the weld pool and use a proportionally higher value of Δp_{max} (6.6x10^6 Pa) at 6 mm/s, the $(d\varepsilon/dT)_{crit}$ curves would still be widely negative.
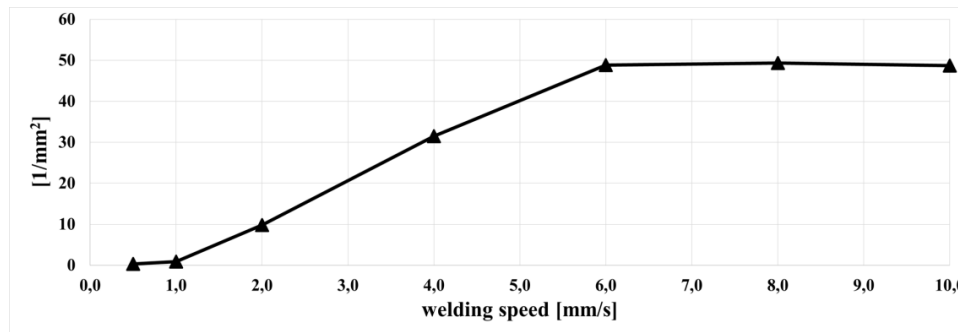

Figure 6. Micro-CT characterisation of total length of the cracks for different welding speeds normalized by the volume of the weld seam

5. Summary and conclusion

Electron beam welding of Mar-M247 has been simulated on the basis of a thermal "heat source" model and of equiaxed as well as columnar initial microstructures obtained by prior microstructure simulations of the solidification and heat treatment process. For two welding experiments with a welding speed of 1 mm/s and 6 mm/s, respectively, a good qualitative agreement between the simulated microstructures and experimental micrographs were found. Furthermore, evaluations of the simulation results using a modified RGB criterion for hot-cracking revealed a significantly higher risk for crack initiation for the higher welding speed for both materials. This is in full agreement with comprehensive experimental cracking statistics for various welding speeds and demonstrates that the presented approach is valid for prediction of hot-cracking under conditions of electron beam welding.

References
[1]   Wheeler A A, Boettinger W J and Mc Fadden G B 1993 *Phys. Rev.* E **47** 1893-909
[2]   Kim S G, Kim W T and Suzuki T 1999 *Phys. Rev.* E **60** 7186-97
[3]   Eiken J, Böttger B and Steinbach I 2006 *Phys. Rev.* E **73** 066122
[4]   David S A, Babu S S and Vitek J M 2003 *JOM* **55** 14.
[5]   MICRESS software, https://web.micress.de
[6]   Böttger B, Grafe U, Ma D and Fries S G 2000 *Mater. Sci. Technol.* **16** 1425-28
[7]   Schmitz G J et al 2012 *Int. J. Adv. Eng. Sci. Appl. Math.* **2** 4 126-39
[8]   Böttger B, Haberstroh C, Giesselmann N 2016 *JOM* **68(1)** 27–36
[9]   Böttger B 2019 *Metall. Mater. Trans.* **50A** 1733
[10]   Rappaz M, Drezet J M and Gremaud M 1999 *Metall. Mater. Trans.* **30A** 449
[11]   Böttger B, Apel M, Santillana B and Eskin D G 2013 *Metall. Mater. Trans.* **44A** 3765-77
[12]   Fang C 2015 *Fusion Engineering and Design*, 2015 357-63
[13]   J. Eiken, Dissertation, Faculty of Georesources and Materials Engineering, RWTH Aachen, ISBN 978-8322-9010-8, 2010.
[14]   Carré A, Böttger B, and Apel M 2014 *J. Crystal Growth* **380** 5–13
[15]   Themo-Calc Software, https://www.thermocalc.com
[16]   Thermotech Ltd. https://www.thermotech.co.uk/databases.html
[17]   Böttger B, Eiken J and Apel M 2009 *J. Comput. Phys.* **228** 6784-95
[18]   Torroba A J et al. 2014 *Integrating Materials and Manufacturing Innovation* **3** 25
[19]   Drezet J M and Allehaux D 2008 *Hot Cracking Phenomena in Welds* vol II, ed T Bollinghaus H Herold C Cross and J Lippold (Springer) pp 19-37